Modulating carbon dots from aggregation-caused quenching to aggregation-induced emission and applying them in sensing, imaging and anti-counterfeiting

Shengtao Zhang, Jinhong Li, Pengyue Xu, Jieyu Zhou, Yan Li, Yongmin Zhang, Shaoping Wu

Modulating carbon dots from aggregation-caused quenching to aggregation-induced emission and applying them in sensing, imaging and anti-counterfeiting

Shengtao Zhang[a,b,§], *Jinhong Li*[c,§], *Pengyue Xu*[a], *Jieyu Zhou*[a], *Yan Li*[b,*], *Yongmin Zhang*[a,d], *Shaoping Wu*[a,*]

[a] *Key Laboratory of Resource Biology and Biotechnology in Western China, Ministry of Education, Biomedicine Key Laboratory of Shaanxi Province, Northwest University, 229 Taibai Road, Xi'an, Shaanxi, 710069, P. R. China.*

[b] *Key Laboratory of Synthetic and Natural Functional Molecule Chemistry of the Ministry of Education, College of Chemistry and Materials Science, Northwest University, Xi'an, 710069, P. R. China.*

[C] *Shaanxi Hantang Pharmaceutical Co., Ltd. Xi'an,710021, P. R. China.*

[d] *Sorbonne Université, CNRS, Institut Parisien de Chimie Moléculaire, UMR 8232, 4 place Jussieu, 75005, Paris, France.*

[§] *These authors contributed equally to this work.*

[*]*Corresponding author: wushaoping@nwu.edu.cn*

ABSTRACT

Aggregation Induced Emission Carbon Dots (AIE-CDs) address the problem of conventional CDs being quenched in the solid-state. However, there are still challenges in comprehending the luminescence mechanism. This work proposed a strategy for preparing green, yellow, and near-infrared CDs by modifying the functional groups on the precursor from hydroxyl and amino to *p*-methylenediamine, in which electronic supply capacity determined the redshift. Additionally, The CDs' properties transformed from Aggregation-Caused Quenching (ACQ) to AIE was realized by substituting non-rotatable hydroxyl or amino groups with the rotatable *p*-

methylenediamine on the precursor. The resulting CDs were then applied in multifield. C-CDs was used for ratiometric detection of Al^{3+} and F^- in pure water through three methods including fluorometer, test strip and smartphone. R-CDs was used for imaging cell nucleus and zebrafish. NIR-CDs (λ_{em}= 676 nm) exhibits dual emission, AIE and phosphorescent characteristics was used for triple anti-counterfeiting and binary information encryption. In summary, our finding presented a strategy for preparing multicolor CDs, proposed a mechanism for the transition of CDs from ACQ to AIE, and explore their multiple applications in anti-counterfeiting, information encapsulation, sensing and imaging.

Keywords: carbon dots, aggregation-induced emission (AIE), aluminum, fluoride; phosphorescence, anti-counterfeiting

1. Introduction

The Nobel prize in chemistry 2023 was awarded to three scientists cultured in quantum dots (QDs), the appearance of QDs adds color to nanotechnology, and quantum effect gives it novel optical and electronic properties different from organic dyes that can be applied in many important fields [1-4]. Carbon dots (CDs) not only inherits the excellent properties of QDs, including emission-dependent excitation, up-conversion photoluminescence, photobleaching and blinking [5, 6], but also solved the disadvantage of greater toxicity of transition metal QDs, and had been widely used in anti-counterfeiting [7, 8], bioimaging [9, 10], drug delivery [11], nanozyme [12-14], catalysis [15, 16] and optical devices [17]. Traditional fluorescent CDs exhibit bright

fluorescence in dispersed state but undergo excessive energy transfer and π-π stacking effects in aggregated state, causing to fluorescence quenching and limiting their practical application [17, 18]. Based on this, researchers prepared aggregation induced emission CDs (AIE CDs) to overcome this limitation [19]. AIE CDs was firstly realized in 2013 by incorporating CDs into a matrix of cetyltrimethylammonium bromide to inhibit the aggregation of CDs [20]. However, AIE CDs obtained by this method still experience quenching at higher concentrations, which still limits its practical applications. In 2019, a solid-state AIE CDs without matrix was obtained by utilizing dithio-2-phenylacetate with rotatable units of disulfide bond as a precursor and this development holds distinct advantages for anti-counterfeiting and bioimaging [21]. Subsequently, many researchers regulated the structure of raw materials to obtain AIE CDs [22], which triggered a wave of research [23-25]. Very recently, yellow solid-state CDs by vibration suppression was prepared from trimellitic acid and piperazine [26]. However, despite some success in the synthesis of AIE CDs, there is still a large gap in insights into their luminescence mechanisms.

Additionally, the luminescence modes of CDs were still single and the wavelength was short, which needs a breakthrough to meet the higher demands in complex application scenarios. Such as anti-counterfeiting and information encapsulation materials need to be easily synthesized, have high production yields, possess a long lifetime, be environmentally friendly and resistant to replication [23, 27-29]. To cater diverse application scenarios, various approaches had been employed

for the synthesis of multicolor CDs encompassing adjustments of the quantity or type of acids, reaction solvents, and proportions of reactants [30-35]. However, there were limited reports on the modulation of fluorescence through subtle changes of functional groups, which is pivotal to explore the luminescence mechanism of CDs.

Aluminum ions (Al^{3+}) and fluoride ions (F^-) play pivotal roles in various fields, while excessive exposure to Al^{3+} can cause damage to the nervous system, and the overuse of F^- can result in fluorosis and dental fluorosis. Literature reported the detection of Al^{3+} using CDs with either AIE enhancement (AIEE) or Aggregation-Caused Quenching (ACQ) characteristics, which suffered from high background interference or pose toxicity concerns due to the use of organic solvents, respectively [36-40], and even CDs with turn on detection face the problem of low yield [41]. Therefore, high yields of CDs and low background detection are two key points to improve the sensing performance and practical ability in the detection of Al^{3+} and F^-. Testing real samples is more complex than laboratory testing and requires simpler sample handling and faster testing. Recently, there has been a notable increase in interest in smartphone-based detection, the portability of the device greatly reduces the detection threshold. Therefore, the integration of the AIE CDs with smartphone to detect Al^{3+} and F^- will further enhance the portability and be more suitable for a wider range of applications.

Herein we present a strategy to obtain multicolor CDs including G-CDs (λ_{em}= 520 nm), Y-CDs (λ_{em}= 553 nm) and NIR-CDs (λ_{em}= 676 nm) by employing

naringenin and acetophenone derivatives as precursors, the acetophenone derivatives differ in the electron-donating capacity of functional groups (-OH, -NH_2, -$N(CH_3)_2$), which determined the fluorescent color of CDs (Fig. 1A). Upon separating NIR-CDs, C-CDs (λ_{em}= 480 nm) and R-CDs (λ_{em}= 602 nm) were obtained. G-CDs and Y-CDs exhibited ACQ properties, while NIR-CDs (λ_{em}= 676 nm) possessed AIE and phosphorescence properties, which was caused by the rotational functional group. These CDs were applied in multifield. Firstly, NIR-CDs was fabricated into fluorescent ink to achieve triple anti-counterfeiting and binary information encryption. Secondly, gram scale of C-CDs was used to detect Al^{3+} and F^- in pure water, which was integrated with test paper and smartphone platform for field detection. Lastly, R-CDs exhibits low cytotoxicity and was successfully used for cellular and zebrafish imaging, thereby demonstrating its potential in bioimaging.

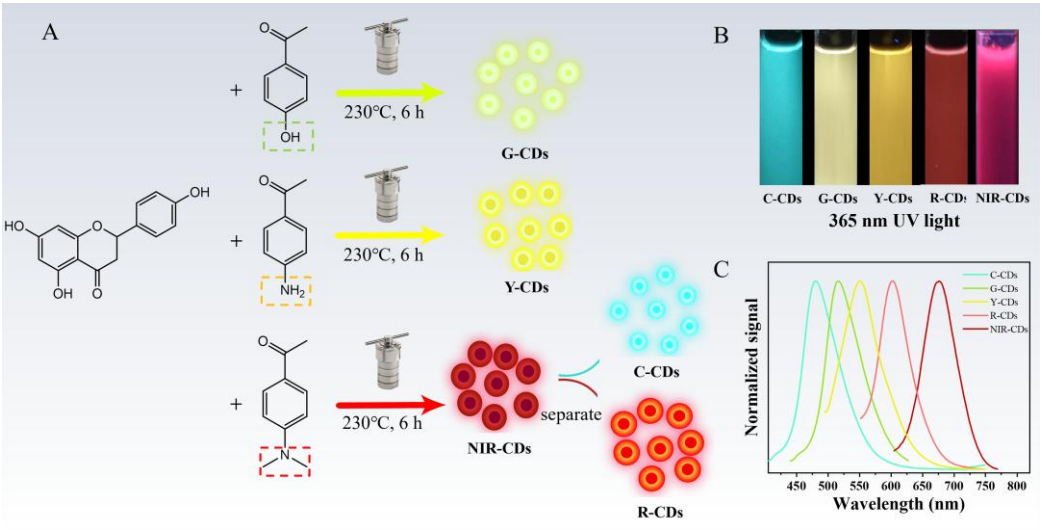

Fig. 1. (A) Synthetic routes of full color CDs; (B) Photographs of C-CDs, G-CDs, Y-CDs, R-CDs and NIR-CDs; (C) Fluorescence emission spectra of C-CDs, G-CDs, Y-CDs, R-CDs and NIR-CDs.

2. Experimental Section

2.1. Synthesis of CDs

Accurately weighed 2.0 g (7.34 mM) of naringin and 1.0 g (7.34 mM) of *p*-hydroxyacetophenone into a 50 mL beaker, completely dissolved with 20 mL of EtOH, which was heated at 230°C for 6 h in a 50 mL Teflon reactor. A yellow clarified solution was obtained and the unreacted small molecules were removed by dialysis (3500 Da) for 48 h. The product G-CDs was obtained after drying at 50℃, and the calculated yield was 10.8%. Y-CDs was synthesized in the same way as G-CDs, except that *p*-hydroxyacetophenone was replaced by *p*-aminoacetophenone, and the yield was 15.7%. NIR-CDs was obtained by the same way except dialysis, with a high yield of 75.7%, after dialysis and column chromatography of NIR-CDs in order, C-CDs and R-CDs were obtained (DCM: MeOH= 80:1, 20:1, 5:1 sequentially) with yields of 47.0% and 5.3%, respectively.

2.2. Calculation of fluorescence quantum yield and fluorescence lifetime

The methods were referred to our previous work [42], the details can be found in the Supporting Information.

2.3. Spectroscopic determination

Weighed 10.0 mg of CDs prepared above and dissolved in 5.0 mL of EtOH to obtain a master batch (2.0 mg/mL), then 50 μL of the master batch was transferred to a colorimetric tube and fixed with EtOH to 5.0 mL to determine the spectral properties. Mixtures of water and EtOH were used to measure the AIE properties of

NIR-CDs and C-CDs. Fluorescence spectra were detected at 405 nm.

2.4. Triple anti-counterfeiting and binary information encryption experiment

To obtain the fluorescent ink (0.5 mg/mL), 5.0 mg of NIR-CDs was accurately weighed and dissolved in 10.0 mL of EtOH. The home-made fluorescent ink was absorbed with a fountain pen and then written on the filter paper. The fluorescent color was observed under a 365 nm UV lamp.

2.5. Al^{3+} and F^- concentration titration experiments

For the titration experiments of Al^{3+}, 50 μL of C-CDs (0.5 mg/mL) was transferred into a 10 mL colorimetric tube, then different volumes of Al^{3+} (1.0 mM, 0, 10, 20, 30, 40, 50, 60, 70 μL) were added and fixed to 5 mL with double-distilled water. For F^- titration experiments, 50 μL of C-CDs was transferred to a 10 mL colorimetric tube, then 70 μL of Al^{3+} (1.0 mM) and various F^- (1.0 mM, 0, 20, 40, 60, 80, 100, 120, 140, 160, 180, 200, 220, 240, 260, 280 μL) were added sequentially and fixed to 5 mL with double-distilled water. The slits were chosen as 5 nm and 10 nm, the voltage was 700 V and the excitation wavelength was set as 375 nm, all fluorescence spectra were measured after the samples were mixed for 5 min.

2.6. Selectivity titration experiments

In the selectivity experiment of C-CDs to Al^{3+}, Al^{3+} was replaced by other possible co-existing ions (1.0 mM, Na^+, Zn^{2+}, Mg^{2+}, K^+, Hg^{2+}, Fe^{3+}, Fe^{2+}, Cu^{2+}, Ca^{2+}, Cu^+, Sn^{2+}, CO_3^{2-}, F^-, S^{2-}, SO_4^{2-}, NO_2^-, Cl^-, Br^-, I^-, CN^-). And in the selectivity experiment of C-CDs-Al^{3+} to F^-, F^- was replaced by above possible co-existing ions.

2.7. Competitive titration experiments

In the competitive experiment of C-CDs to Al^{3+}, 50 μL of C-CDs (5.0 mg/mL), 70 μL of Al^{3+} (1.0 mM) and 70 μL of the above ions were added in sequence to the colorimetric tube and then fixed to 5 mL with double-distilled water to detect their fluorescence spectra. And in the competitive experiment of C-CDs-Al^{3+} to F^-, 50 μL of C-CDs (5.0 mg/mL), 70 μL of Al^{3+} (1.0 mM), 280 μL F^- and 280 μL of the above other ions were added in sequence to the colorimetric tube and then fixed to 5 mL with double-distilled water to detect their fluorescence spectra.

2.8. Al^{3+} test paper

The methods details can be found in the Supporting Information.

2.9. Smartphone sensing platform for Al^{3+} detection

Weighed 1.5 mg of $[Ru(bpy)_3]^{2+}$ dissolved in 5.0 mL of water at a concentration of 0.4 mM. 10 μL $[Ru(bpy)_3]^{2+}$, 30 μL C-CDs, and different volumes of Al^{3+} (1.0 mM, 0, 10, 20, 30, 40, 50, 60, 70, 80 μL) were aspirated and fixed to 5 mL. Fluorescence pictures were taken with a smartphone and the RGB values were detected using the Colorcoll APP.

2.10. Smartphone sensing platform for F^- detection

Weighed 1.5 mg of $[Ru(bpy)_3]^{2+}$ dissolved in 5.0 mL of water at a concentration of 0.4 mM. 10 μL $[Ru(bpy)_3]^{2+}$, 30 μL C-CDs, 80 μL Al^{3+} and different volumes of F^- (1.0 mM, 0, 20, 40, 60, 80, 100, 120, 140, 160, 180, 200, 220, 240, 260, 280, 300 μL) were aspirated and fixed to 5 mL. Fluorescence pictures were taken with a

smartphone and the RGB values were detected using the Colorcoll APP.

2.11. Bioimaging

Bioimaging experiments were performed with reference to our previous work[43], the details can be found in the Supporting Information.

3. Results and Discussions

3.1. Modulating fluorescence of CDs

Using naringenin as main material, G-CDs, Y-CDs and NIR-CDs were prepared by changing the functional groups on acetophenone derivatives from hydroxyl, amino to *p*-methylenediamine. We presume that the modulation of fluorescence is a result of distinct synthetic processes. The inductive effect gradually intensifies with the heightened electron-donating capacity of para-substituted groups. This facilitates the condensation reactions between naringenin and acetophenone derivatives, ultimately increases the degree of conjugation. To confirm the fluorescence modulation wasn’t induced by the acetophenone derivatives itself, CDs synthesized solely from the acetophenone derivatives were conducted. These CDs exhibited blue fluorescence with no redshift (Fig. S5A), which demonstrated the redshift came from the reaction between naringenin and acetophenone derivatives. Furthermore, control experiments demonstrated that the fluorescence of the CDs prepared blue-shifted when the precursor's para-position was altered from formyl group to carboxyl group (Fig. S5B).

3.2. Characterization of CDs

To explore the morphology and structure of CDs, Transmission electron

188 microscopy (TEM) and X-ray powder diffraction (XRD) were employed. As shown in
189 Fig. 2A-B, the average particle sizes of C-CDs, G-CDs, Y-CDs and R-CDs are 2.4 nm,
190 2.3 nm, 2.8 nm, 3.2 nm, respectively, which exhibit a distinct pattern and indicate that
191 the fluorescence modulation of these CDs is follows to Quantum Confinement Effect
192 (QCE). C-CDs and R-CDs show clear lattice structures with a lattice spacing of 0.23
193 nm corresponding to (100) planes of graphite C, while both G-CDs and Y-CDs lack
194 lattice structures that represent amorphous CDs indicate different degrees of reaction
195 compared with C-CDs and R-CDs [44, 45]. This observation was corroborated by the
196 X-ray diffraction (XRD) pattern (Fig. 2C), where C-CDs and R-CDs exhibited peaks
197 at 21°, whereas G-CDs and Y-CDs didn't display obvious peaks. It is hypothesized
198 that this phenomenon is associated with the extent of surface oxidation. The X-ray
199 photoelectron spectroscopy (XPS) indicate that G-CDs and Y-CDs exhibit a lower
200 oxygen content and a higher carbon content in comparison to C-CDs and R-CDs
201 (Table S1), which results in the formation of amorphous CDs.
202 Fourier transform infrared spectra (FT-IR) and XPS were then investigated to
203 affirm the character of these CDs (Fig. 2D). All CDs contained -OH/-NH_2 (~3379 cm^{-1}),
204 -CH_3 (~2923 cm^{-1}), C=C (~1640 cm^{-1}), benzene ring (1500 cm^{-1}~1450 cm^{-1} except
205 G-CDs), C-OH (1200~1000 cm^{-1}). It is noteworthy that C-CDs and R-CDs exhibit
206 stronger absorption peaks in the regions of C=C/C=N, C=O, C-N and benzene rings
207 between 1650 and 800 cm^{-1} compared to G-CDs and Y-CDs. Furthermore, there is an
208 overall enhancement in the FT-IR absorption peaks within this region from G-CDs to

Y-CDs and ultimately to R-CDs, which serves as additional evidence for the gradual increase in the degree of conjugation within CDs. Subsequently, the investigation of the elemental composition of G-CDs, Y-CDs, and R-CDs were carried out by XPS, (Table S1). It was observed that the carbon content from G-CDs, Y-CDs to R-CDs gradually decreased in parallel the oxygen content increased, correlating with the redshift of UV absorption spectra (UV-vis) absorption (Fig. 2E).

To further investigate the properties of these CDs, the fluorescence decay curves (Fig. 2F) and the average amplified fluorescence lifetimes (Table S2) of these CDs were fitted. It can be seen that the fluorescence lifetimes and luminescence efficiencies tend to decrease with the increasing wavelength [46]. And the radiative decay efficiency of G-CDs, Y-CDs and R-CDs gradually increases, with less energy absorbed by the electrons under the same conditions, corresponding to the redshift of fluorescence.

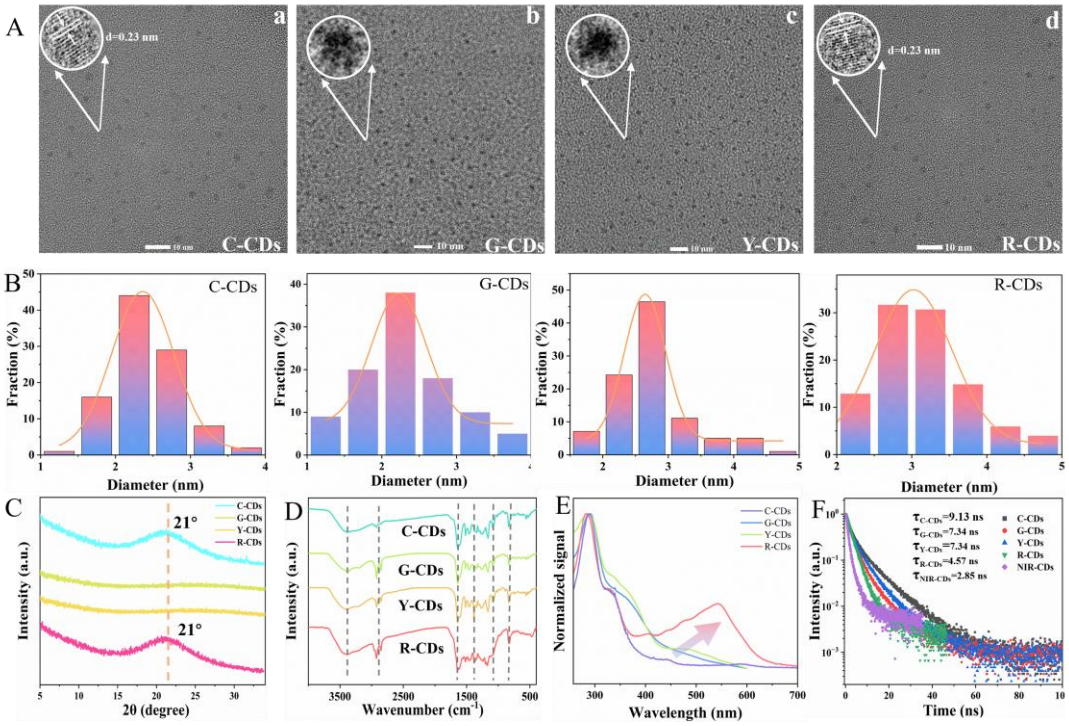

Fig. 2. Characterization of C-CDs, G-CDs, Y-CDs and R-CDs. (A) TEM and HR-TEM (inset) images of C-CDs, G-CDs, Y-CDs, R-CDs are presented from left to right; (B) Particle size distribution plots for C-CDs, G-CDs, Y-CDs and R-CDs are displayed from left to right; (C) XRD patterns of C-CDs, G-CDs, Y-CDs and R-CDs; (D) FT-IR spectra of C-CDs, G-CDs, Y-CDs and R-CDs; (E) UV-vis spectra of C-CDs, G-CDs, Y-CDs and R-CDs; (F) Fluorescence decay curves of C-CDs (λ_{em}= 480 nm), G-CDs (λ_{em}= 520 nm), Y-CDs (λ_{em}= 553 nm), R-CDs (λ_{em}= 602 nm) and NIR-CDs (λ_{em}= 676 nm), respectively.

3.3. Optical properties of synthesized CDs

Table S3 presents the spectral properties of these CDs, which exhibit cyan, green, yellow, red and NIR fluorescence with QYs of 68.8%, 19.2%, 34.3%, 26.9% and 3.5%, respectively. Notably, G-CDs, Y-CDs and R-CDs exhibit ACQ properties, while C-CDs and NIR-CDs with AIE properties. To explore the reason for this transition from ACQ to AIE, a series of experiments were performed next.

NIR-CDs display two emission centers at 480 nm and 676 nm (Fig. 3A), which are both excitation-independent (Fig. S6). To investigate the origin of the dual emission of NIR-CDs, thin-layer chromatography was performed. It was found that NIR-CDs is a mixture of C-CDs (λ_{em}= 480 nm), R-CDs (λ_{em}= 602 nm) and unreacted raw materials (Fig. S7). Fluorescence scans were performed at varying water fractions. As shown in Fig. 3B, the fluorescence intensity of NIR-CDs at 480 nm experienced a decrease as the water fraction increased from 0% to 99%, which was attributed to the quenching of carbon-core caused by excessive resonance energy transfer in the aggregated state. Meanwhile, the NIR fluorescence at 676 nm gradually increased, which is achieved by inhibiting the rotation of *N*,*N*-dimethyl groups on the surface of CDs (Fig. 3C). These findings are supported by the UV absorption spectra (Fig. 3E) and fluorescence lifetime plots. Fig. 3F and Table S4 show a decrease in absorption at 290 nm and 340 nm with increasing water fraction, while absorption at 560 nm gradually increased and red-shifted, confirming the presence of π-π stacking interaction and the formation of *J*-aggregates [21]. The average amplified fluorescence lifetimes of NIR-CDs in Ethanol (EtOH) and in water were 8.96 ns and 2.85 ns, respectively, suggesting that NIR-CDs has different emission centers in water and EtOH [22]. The AIE phenomena was further confirmed by DLS (Table S5). The size of NIR-CDs was 8.7 nm with a zeta potential of -1.7 mV in EtOH. However, in water, the size increased to 31.0 nm and the zeta potential increased to 34.1 mV, which is consistent with the TEM (Fig. S8) and Atomic Force Microscope (AFM)

images. To verify the AIE mechanism of NIR-CDs, control experiments using *p*-aminoacetophenone and *p*-diethylaminobenzaldehyde as acetophenone derivatives were conducted. As depicted in Fig. S9, *p*-aminoacetophenone did not exhibit any AIE properties, whereas *p*-diethylaminobenzaldehyde demonstrated AIE properties. It is suggested that the rotation of *N*,*N*-dimethyl was inhibited by the increasing content of water, which in turn reduced the non-radiative transition and caused AIE. Conversely, the non-rotating amino group could not induce AIE.

It is noteworthy that C-CDs also possesses AIE properties and emits cyan fluorescence in dispersed state and red fluorescence in solid state (Fig. S10 and Fig. S11). Fig. S12A shows that the fluorescence intensity of C-CDs at 480 nm gradually decreased with the increasing of water fraction, while the fluorescence intensity at 600 nm started to increase when the water fraction reached 80%. The AIE properties of C-CDs were verified by UV absorption, DLS, fluorescence lifetime. The UV absorption (Fig. S12B) of C-CDs at 340 nm and 425 nm steadily increases and undergoes a redshift with the increasing of water fraction, indicating the existence of AIE and the formation of *J*-aggregates [21]. Furthermore, C-CDs exhibits size of 2.4 nm in EtOH and 65.2 nm in water, which is consistent with the TEM and AFM images (Fig. S14). Accompanied by zeta potentials of 4.5 mV and -16.9 mV, respectively, this indicates that C-CDs was well dispersed in EtOH but poorly dispersed in water (Table S7). The fluorescence lifetimes of C-CDs in EtOH and water were 9.13 ns and 1.85 ns, respectively (Table S8), demonstrating that C-CDs

has different emission centers in the dispersed and solid states. Furthermore, the maximum emission peak shifts from 480 nm at pH 7.0 to 550 nm at pH 0.2, accompanied by a 595 nm shoulder peak (Fig. S15). The size of C-CDs increased from 2.4 nm to 1258 nm as the pH decreased (Table S7), indicating its aggregation in an acidic environment and the fluorescence color is relative with its degree of aggregation. R-CDs, which use the same raw materials as C-CDs, did not exhibit AIE properties. HR-XPS analysis (Table S6) shows the decrease of N-H and the increase of C-N=C of R-CDs compared to C-CDs, indicating an increasing conjugate structure and degree of reaction from C-CDs to R-CDs. This means that C-CDs has more starting functional groups (-$N(CH_3)_2$) on its surface, while R-CDs is more reactive and carry less -$N(CH_3)_2$, leading to ACQ properties.

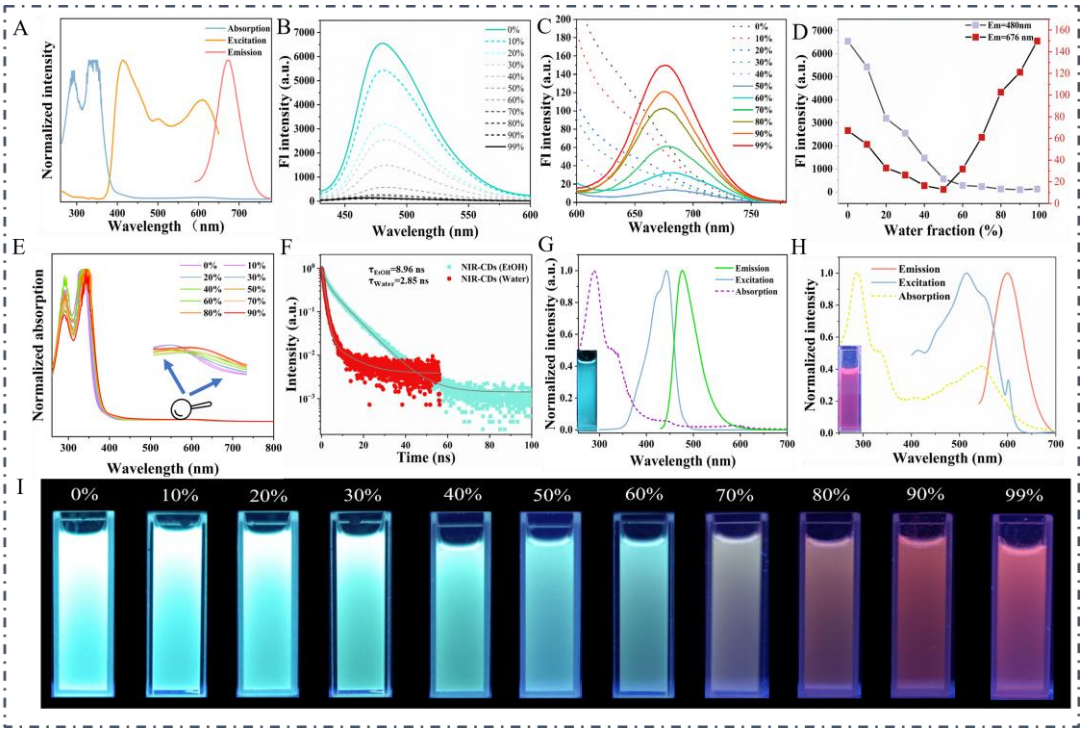

Fig. 3. Optical properties of NIR-CDs. (A) Absorption (blue), excitation (orange) and emission (red) curves of NIR-CDs; (B) Fluorescence emission curves of NIR-CDs at 480 nm in different

water contents (λ_{ex}= 405 nm); (C) Fluorescence emission curves of NIR-CDs at 676 nm in different water contents (λ_{ex}= 405 nm); (D) Fluorescence intensity of NIR-CDs at 480 nm (purple line) and 676 nm (red line) at different water contents; (E) Absorption spectra of NIR-CDs with different water contents; (F) Fluorescence decay curves of NIR-CDs in EtOH (λ_{em} =480 nm) and water (λ_{em}= 676 nm), respectively; (G) Absorption (purple), excitation (blue) and emission (green) curves of C-CDs; (H) Absorption (yellow), excitation (blue) and emission (red) curves of C-CDs; (I) Fluorescence photos of NIR-CDs at different water contents (0%-99%) under 365 nm UV lamp.

3.4. Swiss knife applications of CDs

3.4.1. Feasibility study of Al^{3+} and F^- sensing

Based on the AIE properties, high yield and Al^{3+}-trigged aggregation of C-CDs, a strong practically probe to detect Al^{3+} and F^- was developed. Table S9 and Table S10 demonstrate the comparative performance of Al^{3+} and F^- among C-CDs and reported probes, the working detection process exhibited low toxicity and higher sensitivity. Fig. 4A shows the fluorescence intensity of C-CDs at 480 nm gradually increased after the addition of Al^{3+}, accompanied by a redshift to 505 nm. C-CDs exhibits red fluorescence in pure water, while Al^{3+} enhanced the green fluorescence, showing good linearity between 0-14 μM (R^2= 0.9963), and the limit of detection (LOD) was 0.081 μM. Some potential coexisting ions were used to detect the selectivity and competitiveness of C-CDs. As shown in Fig. 4C, these ions didn't cause a significant increase in fluorescence. In competitive experiments, almost no interference was observed from substances other than Fe^{3+}, which caused a 37.3% reduction in the

fluorescence of C-CDs-Al^{3+}. To solve this problem, the masking agent ascorbic acid was introduced into the system, which can reduce Fe^{3+} to Fe^{2+} (Fig. S19). Accuracy assessment experiments exhibited a high degree of overlap with reference method (Table S11).

The stability and kinetics of C-CDs in response to Al^{3+} were next investigated, C-CDs responds well to Al^{3+} at high ionic strength (NaCl concentration of 200 mM). Kinetic experiment was shown in Fig. S20, where the response of C-CDs to Al^{3+} could reach stability at 4 min with a 9-fold increase in fluorescence intensity. The response of C-CDs-Al^{3+} to F^- was verified based on the chelation reaction of Al^{3+} and F^-, and F^- restored the fluorescence of C-CDs-Al^{3+} from green to red (Fig. 4D). The analytical response of C-CDs-Al^{3+} to F^- show good linearity between 0-28 μM (R^2= 0.9994) and 30-56 μM (R^2= 0.9996) [47], with a LOD of 0.67 μM (Fig. 4E). Fig. 4F shows good selectivity of C-CDs-Al^{3+} to detect F^-.

Finally, a possible mechanism was proposed that C-CDs aggregates in water to emit red fluorescence, while Al^{3+} can chelate with hydroxyl groups on C-CDs, then entrapping between C-CDs and reducing its aggregation to emit green fluorescence, while F^- takes away Al^{3+} and the fluorescence returns to red (Fig. 4G). To validate this mechanism, the size of C-CDs in different systems were investigated (Table S7), the size of C-CDs in water was 65.2 nm, while reached 481.5 nm when Al^{3+} was present, providing evidence that Al^{3+} chelate with hydroxyl groups and insert between C-CDs to prevent the aggregation among C-CDs. Additionally, owing to the structural

similarity between R-CDs and C-CDs, Al^{3+} is also capable of inducing aggregation of R-CDs (Fig. S21). Since R-CDs didn't has AIE properties, the addition of Al^{3+} leads to (ACQ). Fluorescence decay curves demonstrate that the lifetime of C-CDs at τ_2 remained, while τ_1 increased from 0.551 ns to 0.827 ns after the addition of Al^{3+}, which revealed a reduction in the degree of aggregation of C-CDs (Table S12 and Fig. S22). Above observation proved that the addition of Al^{3+} reduces the aggregation of C-CDs.

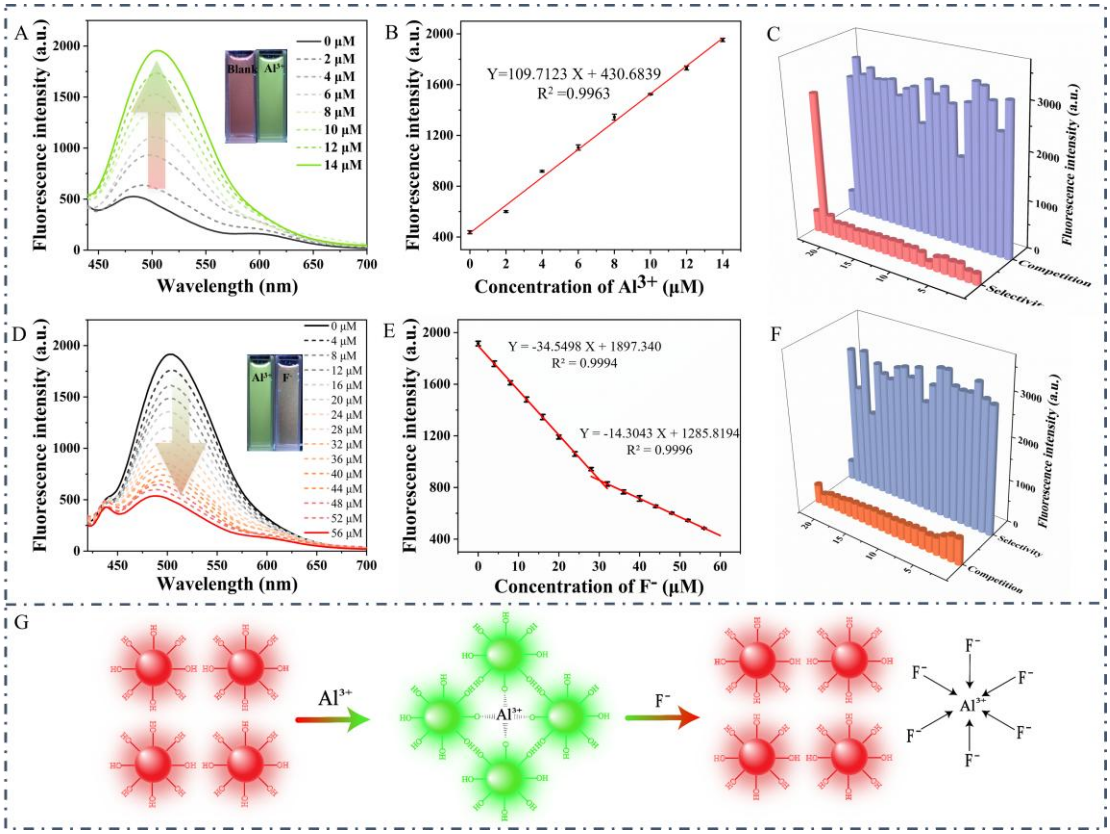

Fig. 4. (A) Fluorescence emission curves of C-CDs with the addition of Al^{3+} (0-14 μM); (B) Linearity of concentration of Al^{3+} and fluorescence intensity; (C) Fluorescence emission intensity of C-CDs (purple bar) and C-CDs+Al^{3+} (14 μM, red bar) in the presence of Zn^{2+}, Sn^{2+}, Pb^{2+}, Mg^{2+}, Na^{+}, K^{+}, Fe^{3+}, Ba^{2+}, Ca^{2+}, Co^{2+}, Cu^{+}, Fe^{2+}, Cu^{2+}, CO_3^{2-}, F^{-}, S^{2-}, SO_4^{2-}, NO_2^{-}, Cl^{-}, Br^{-}, I^{-}, CN^{-}; (D) Fluorescence emission curves of C-CDs+Al^{3+} (14 μM) with different concentrations of F^{-} (0-56

μM); (E) Linearity of concentration of F^- and fluorescence intensity; (F) Fluorescence emission intensity of C-CDs+Al^{3+} (blue bar) and C-CDs+Al^{3+}+ F^- (14 μM, red bar) in the presence of Zn^{2+}, Sn^{2+}, Pb^{2+}, Mg^{2+}, Na^+, K^+, Fe^{3+}, Ba^{2+}, Ca^{2+}, Co^{2+}, Cu^+, Fe^{2+}, Cu^{2+}, CO_3^{2-}, S^{2-}, SO_4^{2-}, NO_2^-, Cl^-, Br^-, I^-, CN^-; (G) Possible response mechanism diagram of C-CDs toward $Al^{3+}$and F^-.

3.4.2. Field detection of Al^{3+} and F^-

The fluorescence method is more sensitive and accurate, but it requires complicated instrumentation to test, which is not suitable to field analysis. Therefore, two methods for the rapid detection of Al^{3+} and F^- were proposed. Firstly, test paper for Al^{3+} was prepared (Fig. 5A), the control group showed red fluorescence, while the addition of Al^{3+} changed red fluorescence to green and enhanced gradually. For more sensitive detection, C-CDs was combined with Nile Red to enable ratiometric detection of Al^{3+}, which resulted in a more intuitive display of Al^{3+}-induced fluorescence color change (Fig. 5B). In addition, selectivity and competitiveness experiments were conducted, demonstrating high selectivity and anti-interference (Fig. 5C and Fig. S23). To enhance the detection sensitivity and visualization of Al^{3+} and F^- concentrations, a method to visualize Al^{3+} and F^- concentrations with smartphone was developed. As shown in Fig. 5D and 5E, Al^{3+} alters the fluorescence from red to green, while F^- alters the fluorescence from green to red. The RGB values were captured with a smartphone and plotted against the concentrations of Al^{3+} and F^- using B/R with R^2 of 0.9970 and 0.9971 (Fig. 5F and 5G), respectively. The smartphone sensing platform based on C-CDs demonstrated good sensing performance, which is expected

368 to be used for the fast detection of Al^{3+} and F^-.

369 *3.4.3. Detection of Al^{3+} and F^- in lake water.*

370 The insoluble impurities in the lake water were removed by filtration, and then
371 ascorbic acid was added to remove Fe^{3+} . C-CDs was used to detect Al^{3+} and F^- in real
372 samples (Table 1). The standard recovery rate of C-CDs for the detection of Al^{3+} was
373 in the range of 98.0-104.0%, with relative standard deviations below 2.6%. For F^-
374 assay, the standard recovery rate was in the range of 98.2-100.2%, with relative
375 standard deviations below 3.5%. The results demonstrated the ability of C-CDs to
376 detect Al^{3+} and F^- in real samples.

377 **Table 1.** Proposed method used to detect Al^{3+} and F^- in lake water

Testing items	added (μM)	Measured (μM)	Recovery (%)	RSD (%)
Al^{3+}	2.0	2.08	104.0	2.6%
	7.0	6.95	99.3	1.2%
	12.0	11.76	98.0	1.9%
F^-	20.0	19.89	99.5	1.7%
	30.0	30.07	100.2	0.9%
	40.0	39.29	98.2	3.5%

378 *3.4.4. Bioimaging*

379 Due to the longer wavelength and brighter fluorescence QYs, R-CDs has been
380 applied to cellular imaging. As shown in Fig. 5H, R-CDs emits bright fluorescence in
381 HepG2 cells and has enhanced brightness in the nucleus, suggesting its potential for
382 nuclear staining [48]. Furthermore, R-CDs demonstrates superior tissue penetration
383 capabilities and has been applied in zebrafish imaging (Fig. 5I). The cytotoxicity of
384 both R-CDs and C-CDs was minimal, the cell survival rate of HepG2 reached 98%

when the concentration of R-CDs or C-CDs was 200.0 μg/mL (Fig. S24). In conclusion, R-CDs is a potentially nanoprobe that can be used for bioimaging.

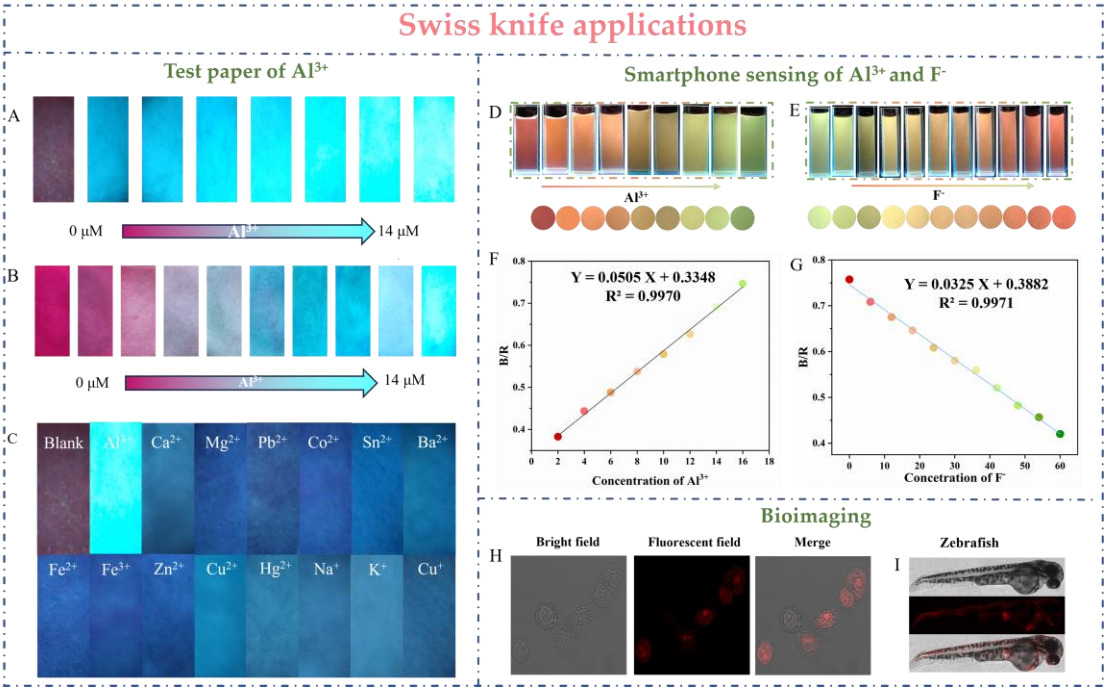

Fig. 5. (A) Test paper of Al^{3+} under different concentrations of Al^{3+}; (B) Ratiometric test paper of Al^{3+} under different concentrations of Al^{3+}; (C) Test paper of C-CDs immersed in various ions; (D) Photos of C-CDs and $[Ru(bpy)_3]^{2+}$ in the addition of Al^{3+} (0-16 μM); (E) Photos of C-CDs and $[Ru(bpy)_3]^{2+}$ with 16 μM Al^{3+} in the addition of F^- (0-60 μM); (F) Linearity of concentration of Al^{3+} and B/R; (G) Linearity of concentration of F^- and B/R; (H) Fluorescent confocal photographs of HepG2 cells in the presence of R-CDs (10.0 μg/mL); (I) Fluorescent confocal photographs of zebrafish in the presence of R-CDs (10.0 μg/mL).

3.4.5. Triple anti-counterfeiting and binary information encryption

NIR-CDs was made it into a triple anti-counterfeit ink due to its fascinating optical properties. As shown in Fig. 6A, writing on the filter paper with a pen filled with fluorescent ink is not visible under daylight. However, due to the aggregation of

NIR-CDs on the filter paper, it emitted red fluorescence under 365 nm UV lamp, constituting the first layer of anti-counterfeiting. Spraying water onto the filter paper disperses NIR-CDs and generates blue fluorescence, representing the second level of anti-counterfeiting. The change in fluorescence color from cyan to blue may be attributed to the physical interaction between NIR-CDs and the filter paper[40]. After the filter paper dries and the UV lamp was turned off, a green phosphorescence lasting for 7 seconds could be observed (Fig. 6B), constituting the third level of anti-counterfeiting. Phosphorescence forms due to the filter paper restricts the motion of NIR-CDs and facilitates the stabilization of excited triplet electrons[49, 50].

Furthermore, a binary-to-decimal information encryption system was developed. The code number '1010011010' was sprayed with NIR-CDs, R-CDs, or a mixture of both (Fig. 6C). Upon turning on the UV lamp, red fluorescence was employed to display the numeral "1010011010". After activating the water spray system, the digit '11000' was showcased using pink fluorescence. Finally, upon deactivating the light source, the numeral '1101010' was indicated using green fluorescence. Convert these numbers into decimal codes corresponding to 666, 12 and 106. Furthermore, it is possible to change the coloring agent to modify the code, and different combinations of codes can be obtained by changing the sequence of turning the light on and off. Due to the flexibility and complexity of the secure system, it is almost impossible to break it without getting the correct order.

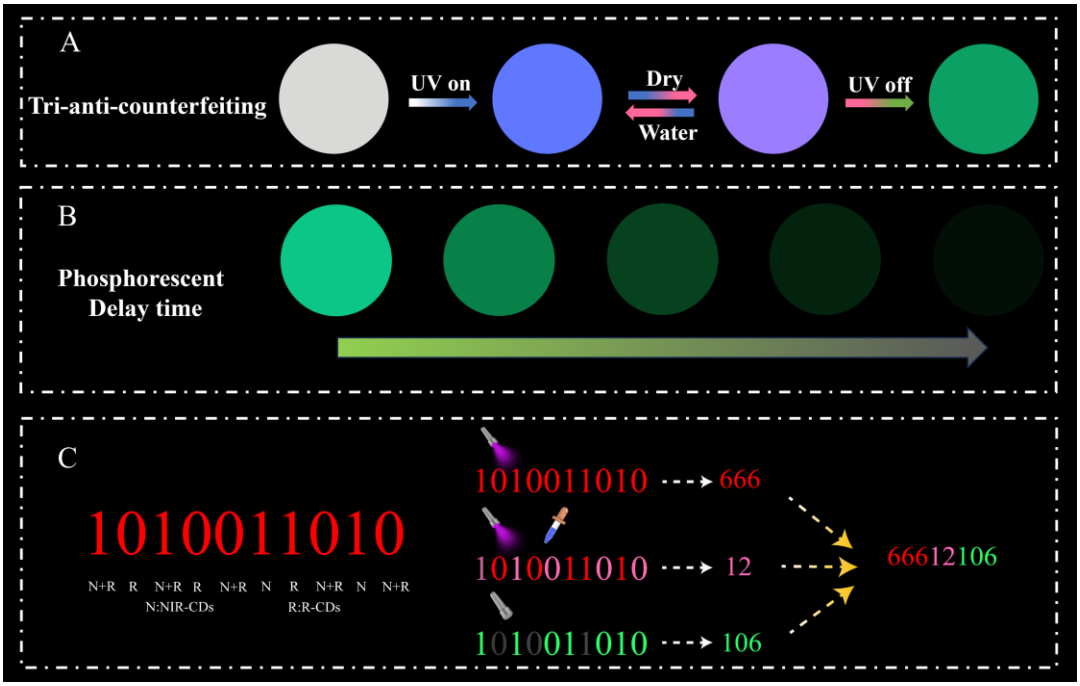

Fig. 6. Triple anti-counterfeiting and information encryption of NIR-CDs. (A) Tri-anti-counterfeiting of NIR-CDs on filter paper; (B) Phosphorescent duration of NIR-CDs on filter paper; (C) Binary information encryption system diagram.

4. Conclusion

In conclusion, we prepared cyan, green, yellow, red, and near-infrared CDs using naringenin and acetophenone derivatives as raw materials. Characterization and control experiments demonstrated that the color of the CDs can be modulated by the electron supplying ability of functional group. Furthermore, a method for producing AIE CDs was proposed, and it was discovered that the CDs underwent a transition from ACQ to AIE when the functional group of the precursor changed from a non-rotatable -OH or $-NH_2$ to a rotatable $-N(CH_3)_2$. These CDs exhibit excellent optical properties and have been applied in various fields. NIR-CDs was employed in ink for triple anti-counterfeiting and binary information encryption. C-CDs was used for

ratiometric quantitative sensing of Al^{3+} and F^- using portable devices such as smartphone and test paper. R-CDs was successfully used for cellular and zebrafish imaging, demonstrating its potential in the field of bioimaging applications. This work offers a new approach for comprehending the mechanism of AIE CDs and lays a foundation for the development of AIE CDs.

CRediT authorship contribution statement

Shengtao Zhang: Conceptualization, Investigation, Formal analysis, Writing-original draft. **Jinhong Li**: Conceptualization, Funding acquisition, Writing-original draft. **Pengyue Xu**: Investigation, Methodology. **Jieyu Zhou**: Writing-review & editing. **Yan Li**: Writing-review & editing, Funding acquisition, Resources. **Yongmin Zhang**: Writing-review & editing. **Shaoping Wu**: Writing-review & editing, Funding acquisition, Resources.

Conflict of Interest

There are no conflicts to declare.

Acknowledgements

This work was supported by the National Natural Science Foundation of China (No. 22074119), the Key Research and Development Program of Shaanxi Province (No. 2021ZDLSF03-03), Biomedicine Key Laboratory of Shaanxi Province (No. 2018SZS41).

References

[1] R. Rossetti, S. Nakahara, L. Brus, Quantum size effects in the redox potentials, resonance Raman spectra, and electronic spectra of CdS crystallites in aqueous solution, J. Chem. Phys.

79(2) (1983) 1086-1088, 10.1063/1.445834.

[2] H. Lu, G. Carroll, N. Neale, M. Beard, infrared quantum dots: progress, challenges, and opportunities, ACS Nano. 13(2) (2019) 939-953, 10.1021/acsnano.8b09815.

[3] F. García de Arquer, D. Talapin, V. Klimov, Y. Arakawa, M. Bayer, E. Sargent, Semiconductor quantum dots: technological progress and future challenges, Science. 373(6555) (2021) eaaz8541, doi:10.1126/science.aaz8541.

[4] H. Guo, Y. Lu, Z. Lei, H. Bao, M. Zhang, Z. Wang, C. Guan, B. Tang, Z. Liu, L. Wang, Machine learning-guided realization of full-color high-quantum-yield carbon quantum dots, Nat. Commun. 15(1) (2024) 4843, 10.1038/s41467-024-49172-6.

[5] X. Xu, R. Ray, Y. Gu, H. Ploehn, L. Gearheart, K. Raker, W. Scrivens, Electrophoretic analysis and purification of fluorescent single-walled carbon nanotube fragments, J. Am. Chem. Soc. 126(40) (2004) 12736-12737, 10.1021/ja040082h.

[6] Z. Yang, T. Xu, H. Li, M. She, J. Chen, Z. Wang, S. Zhang, J. Li, Zero-dimensional carbon nanomaterials for fluorescent sensing and imaging, Chem. Rev. 123(18) (2023) 11047-11136, 10.1021/acs.chemrev.3c00186.

[7] X. Yu, H. Zhang, J. Yu, Luminescence anti-counterfeiting: from elementary to advanced, Aggregate. 2(1) (2021) 20-34, https://doi.org/10.1002/agt2.15.

[8] Q. Feng, Z. Xie, M. Zheng, Room temperature phosphorescent carbon dots for latent fingerprints detection and in vivo phosphorescence bioimaging, Sens. Actuators B Chem. 351 (2022) 130976, https://doi.org/10.1016/j.snb.2021.130976.

[9] C. Zhou, R. Cheng, B. Liu, Y. Fang, K. Nan, W. Wu, Y. Xu, Cascade selective recognition of H_2O_2 and ascorbic acid in living cells using carbon-based nanozymes with peroxidase-like activity, Sens. Actuators B Chem. 402 (2024) 135118, https://doi.org/10.1016/j.snb.2023.135118.

[10] J. Yang, H. Liu, Y. Huang, L. Li, X. Zhu, Y. Ding, One-step hydrothermal synthesis of near-infrared emission carbon quantum dots as fluorescence aptamer sensor for cortisol sensing and imaging, Talanta. 260 (2023) 124637, https://doi.org/10.1016/j.talanta.2023.124637.

[11] M. Liu, B. Chen, C. Li, C. Huang, Carbon dots: synthesis, formation mechanism,

fluorescence origin and sensing applications, Green Chem. 21(3) (2019) 449-471, 10.1039/C8GC02736F.

[12] G. Hutton, B. Reuillard, B. Martindale, C. Caputo, C. Lockwood, J. Butt, E. Reisner, Carbon dots as versatile photosensitizers for solar-driven catalysis with redox enzymes, J. Am. Chem. Soc. 138(51) (2016) 16722-16730, 10.1021/jacs.6b10146.

[13] L. Haiyang, L. Guantong, Z. Nan, Y. Zhanye, J. Xinge, Z. Bing, Y. Tian, Ag-carbon dots with peroxidase-like activity for colorimetric and SERS dual mode detection of glucose and glutathione, Talanta. 273 (2024) 125898, https://doi.org/10.1016/j.talanta.2024.125898.

[14] Y. Zhu, R. Zhang, Z. Hu, F. Wu, B, N co-doped carbon dots as efficient nanozymes for colorimetric and fluorometric dual-mode detection of cholesterol, Talanta. 278 (2024) 126471, https://doi.org/10.1016/j.talanta.2024.126471.

[15] H. Guo, J. Raj, Z. Wang, T. Zhang, K. Wang, L. Lin, W. Hou, J. Zhang, M. Wu, J. Wu, L. Wang, Synergistic effects of amine functional groups and enriched-atomic-iron sites in carbon dots for industrial-current–density CO_2 electroreduction, Small. 20(32) (2024) 2311132, https://doi.org/10.1002/smll.202311132.

[16] B. Hu, K. Huang, B. Tang, Z. Lei, Z. Wang, H. Guo, C. Lian, Z. Liu, L. Wang, Graphene quantum dot-mediated atom-layer semiconductor electrocatalyst for hydrogen evolution, Nanomicro Lett. 15(1) (2023) 217, 10.1007/s40820-023-01182-7.

[17] B. Wang, S. Lu, The light of carbon dots: from mechanism to applications, Matter. 5(1) (2022) 110-149, https://doi.org/10.1016/j.matt.2021.10.016.

[18] H. Li, Y. Chen, H. Wang, H. Wang, Q. Liao, S. Han, Y. Li, D. Wang, G. Li, Y. Deng, Amide (n, π*) transitions enabled clusteroluminescence in solid-state carbon dots, Adv. Funct. Mater. 33(37) (2023) 2302862, https://doi.org/10.1002/adfm.202302862.

[19] Y. Jia, Z. Cheng, G. Wang, S. Shuang, Y. Zhou, C. Dong, F. Du, Nitrogen doped biomass derived carbon dots as a fluorescence dual-mode sensing platform for detection of tetracyclines in biological and food samples, Food Chem. 402 (2023) 134245, https://doi.org/10.1016/j.foodchem.2022.134245.

[20] M. Gao, C. Liu, Z. Wu, Q. Zeng, X. Yang, W. Wu, Y. Li, C. Huang, A surfactant-assisted

redox hydrothermal route to prepare highly photoluminescent carbon quantum dots with aggregation-induced emission enhancement properties, Chem. Commun. 49(73) (2013) 8015-8017, 10.1039/C3CC44624G.

[21] H. Yang, Y. Liu, Z. Guo, B. Lei, J. Zhuang, X. Zhang, Z. Liu, C. Hu, Hydrophobic carbon dots with blue dispersed emission and red aggregation-induced emission, Nat. Commun. 10(1) (2019) 1789, 10.1038/s41467-019-09830-6.

[22] X. Xu, L. Mo, Y. Li, X. Pan, G. Hu, B. Lei, X. Zhang, M. Zheng, J. Zhuang, Y. Liu, C. Hu, Construction of carbon dots with color-tunable aggregation-induced emission by nitrogen-induced intramolecular charge transfer, Adv. Mater. 33(49) (2021) 2104872, https://doi.org/10.1002/adma.202104872.

[23] Y. Ru, G. Waterhouse, S. Lu, Aggregation in carbon dots, Aggregate. 3(6) (2022) e296, https://doi.org/10.1002/agt2.296.

[24] S. Zhang, B. Li, J. Zhou, J. Shi, Z. He, Y. Zhao, Y. Li, Y. Shen, Y. Zhang, S. Wu, Kill three birds with one stone: Mitochondria-localized tea saponin derived carbon dots with AIE properties for stable detection of HSA and extremely acidic pH, Food Chem. 405 (2023) 134865, https://doi.org/10.1016/j.foodchem.2022.134865.

[25] Z. Yang, H. Li, T. Xu, M. She, J. Chen, X. Jia, P. Liu, X. Liu, J. Li, Red emissive carbon dots as a fluorescent sensor for fast specific monitoring and imaging of polarity in living cells, J. Mater. Chem. A. 11(6) (2023) 2679-2689, 10.1039/D2TA09462B.

[26] Z. Wan, Y. Li, Y. Zhou, D. Peng, X. Zhang, J. Zhuang, B. Lei, Y. Liu, C. Hu, High-efficiency solid-state luminescence from hydrophilic carbon dots with aggregation-induced emission characteristics, Adv. Funct. Mater. 33(11) (2023) 2207296, https://doi.org/10.1002/adfm.202207296.

[27] K. Muthamma, D. Sunil, P. Shetty, Carbon dots as emerging luminophores in security inks for anti-counterfeit applications - an up-to-date review, Appl. Mater. 23 (2021) 101050, https://doi.org/10.1016/j.apmt.2021.101050.

[28] S. Zhang, J. Wang, Y. Ni, Y. Li, H. Zhang, W. Zhang, Z. Xie, S. Zhou, Modulation of carbon dots hybrids lasers for high security flexible multi-level anti-counterfeiting, J. Alloys Compd.

957 (2023) 170307, https://doi.org/10.1016/j.jallcom.2023.170307.

[29] Y. Wang, X. Li, S. Zhao, B. Wang, X. Song, J. Xiao, M. Lan, Synthesis strategies, luminescence mechanisms, and biomedical applications of near-infrared fluorescent carbon dots, Coordin Chem Rev. 470 (2022) 214703, https://doi.org/10.1016/j.ccr.2022.214703.

[30] L. Wang, W. Li, L. Yin, Y. Liu, H. Guo, J. Lai, Y. Han, G. Li, M. Li, J. Zhang, R. Vajtai, P. Ajayan, M. Wu, Full-color fluorescent carbon quantum dots, Sci. Adv. 6(40) (2020) eabb6772, doi:10.1126/sciadv.abb6772.

[31] Z. He, Y. Sun, C. Zhang, J. Zhang, S. Liu, K. Zhang, M. Lan, Recent advances of solvent-engineered carbon dots: a review, Carbon. 204 (2023) 76-93, https://doi.org/10.1016/j.carbon.2022.12.052.

[32] J. Wang, J. Zheng, Y. Yang, X. Liu, J. Qiu, Y. Tian, Tunable full-color solid-state fluorescent carbon dots for light emitting diodes, Carbon. 190 (2022) 22-31, https://doi.org/10.1016/j.carbon.2022.01.001.

[33] K. Jiang, S. Sun, L. Zhang, Y. Lu, A. Wu, C. Cai, H. Lin, Red, green, and blue luminescence by carbon dots: full-color emission tuning and multicolor cellular imaging, Angew. Chem. Int. Ed. 54(18) (2015) 5360-5363, https://doi.org/10.1002/anie.201501193.

[34] L. Ai, Z. Song, M. Nie, J. Yu, F. Liu, H. Song, B. Zhang, G. Waterhouse, S. Lu, Solid-state fluorescence from carbon dots widely tunable from blue to deep red through surface ligand modulation, Angew. Chem. Int. Ed. 62(12) (2023) e202217822, https://doi.org/10.1002/anie.202217822.

[35] S. Wang, Y. Wang, Y. Ning, W. Wang, Q. Liu, Multicolor emissive carbon dot-based fluorometric analysis platform for rapid quantification and discrimination of nitroimidazole antibiotic residues, Talanta. 271 (2024) 125679, https://doi.org/10.1016/j.talanta.2024.125679.

[36] Y. Sang, K. Wang, X. Kong, F. Cheng, C. Zhou, W. Li, Color-multiplexing europium doped carbon dots for highly selective and dosage-sensitive cascade visualization of tetracycline and Al^{3+}, Sens. Actuators B Chem. 362 (2022) 131780, https://doi.org/10.1016/j.snb.2022.131780.

[37] J. Liu, Y. Zhan, B. Qiu, Z. Lin, L. Guo, Portable smartphone platform based on aggregation-

induced enhanced emission carbon dots for ratiometric quantitative sensing of fluoride ions, ACS Sens. 8(2) (2023) 884-892, 10.1021/acssensors.2c02589.

[38] X. Li, L. Zhao, Y. Wu, A. Zhou, X. Jiang, Y. Zhan, Z. Sun, Nitrogen and boron co-doped carbon dots as a novel fluorescent probe for fluorogenic sensing of Ce^{4+} and ratiometric detection of Al^{3+}, Spectrochim. Acta. A. 282 (2022) 121638, https://doi.org/10.1016/j.saa.2022.121638.

[39] X. Tang, Y. Zhao, H. Yu, S. Cui, H. Temple, E. Amador, Y. Gao, M. Chen, S. Wang, Z. Hu, W. Chen, Concentration-regulated multi-color fluorescent carbon dots for the detection of rifampicin, morin and Al^{3+}, Mater. Today Adv. 18 (2023) 100383, https://doi.org/10.1016/j.mtadv.2023.100383.

[40] X. Bao, E.V. Ushakova, E. Liu, Z. Zhou, D. Li, D. Zhou, S. Qu, A.L. Rogach, On–off switching of the phosphorescence signal in a carbon dot/polyvinyl alcohol composite for multiple data encryption, Nanoscale. 11(30) (2019) 14250-14255, 10.1039/C9NR05123F.

[41] L. Yan, B. Zhang, Z. Zong, W. Zhou, S. Shuang, L. Shi, Artificial intelligence-integrated smartphone-based handheld detection of fluoride ion by Al^{3+}-triggered aggregation-induced red-emssion enhanced carbon dots, J. Colloid Interface Sci. 651 (2023) 59-67, https://doi.org/10.1016/j.jcis.2023.07.125.

[42] W. Zhao, P. Xu, Y. Ma, Y. Song, Y. Wang, P. Zhang, B. Li, Y. Zhang, J. Li, S. Wu, Old trees bloom new flowers, lysosome targeted near-infrared fluorescent probe for ratiometric sensing of hypobromous acid in vitro and in vivo based on Nile red skeleton, Bioorg. Chem. 143 (2024) 107031, https://doi.org/10.1016/j.bioorg.2023.107031.

[43] W. Zhao, S. Zhang, J. Yan, P. Xu, B. Li, Y. Zhang, J. Li, S. Wu, A dual-emission fluorescent probe for simultaneous detection of singlet oxygen and hypochlorous acid in lipid droplets, Sens. Actuators B Chem. 412 (2024) 135813, https://doi.org/10.1016/j.snb.2024.135813.

[44] Y. Yang, N. Xiao, S. Liu, L. Han, N. Li, H. Luo, pH-induced aggregation of hydrophilic carbon dots for fluorescence detection of acidic amino acid and intracellular pH imaging, Mater. Sci. Eng: C. 108 (2020) 110401, https://doi.org/10.1016/j.msec.2019.110401.

[45] M. Liu, L. Yang, R. Li, B. Chen, H. Liu, C. Huang, Large-scale simultaneous synthesis of

highly photoluminescent green amorphous carbon nanodots and yellow crystalline graphene quantum dots at room temperature, Green Chem. 19(15) (2017) 3611-3617, 10.1039/C7GC01236E.

[46] Z. Wang, F. Yuan, X. Li, Y. Li, H. Zhong, L. Fan, S. Yang, 53% Efficient red emissive carbon quantum dots for high color rendering and stable warm white-light-emitting diodes, Adv. Mater. 29(37) (2017) 1702910, https://doi.org/10.1002/adma.201702910.

[47] S. Zhang, Y. Gu, Z. Shi, N. Lu, H. Xu, A novel reversible fluorescent probe based on naphthalimide for sequential detection of aluminum (Al^{3+}) and fluoride (F^{-}) ions and its applications, Anal Methods. 13(44) (2021) 5360-5368, 10.1039/D1AY01545A.

[48] H. Liu, X. Geng, X. Wang, L. Wei, Z. Li, S. Lin, L. Xiao, A carbonized fluorescent nucleolus probe dscloses RNA reduction in the process of mitophagy, CCS Chem. 4(8) (2022) 2698-2710, doi:10.31635/ccschem.021.202101371.

[49] J. Tan, J. Zhang, W. Li, L. Zhang, D. Yue, Synthesis of amphiphilic carbon quantum dots with phosphorescence properties and their multifunctional applications, J. Mater. Chem. C. 4(42) (2016) 10146-10153, 10.1039/C6TC03027K.

[50] M. Fu, L. Lin, X. Wang, X. Yang, Hydrogen bonds and space restriction promoting long-lived room-temperature phosphorescence and its application for white light-emitting diodes, J. Colloid Interface Sci. 639 (2023) 78-86, https://doi.org/10.1016/j.jcis.2023.02.040.